Several Computational Aeroacoustics solutions for the ducted diaphragm at low Mach number

Mélanie Piellard*
Delphi Thermal Systems
L-4940 Bascharage, Luxembourg

Christophe Bailly†
Laboratoire de Mécanique des Fluides et d'Acoustique
École Centrale de Lyon & UMR CNRS 5509, 69134 Ecully, France
& Institut Universitaire de France

A hybrid method of aeroacoustic noise computation based on Lighthill's Acoustic Analogy is applied to investigate the noise radiated by a low Mach number flow through a ducted diaphragm. The simulation method is a two-step hybrid approach relying on Lighthill's acoustic analogy, assuming the decoupling of noise generation and propagation. The first step consists of an incompressible Large Eddy Simulation of the turbulent flow field, during which aerodynamic quantities are recorded. In the second step, a variational formulation of Lighthill's Acoustic Analogy using a finite element discretization is solved in the Fourier space. The sensitive steps consisting in computing and transferring source term data from the fluid mesh to the acoustic mesh are reviewed. Indeed, as fluid and acoustic meshes have different constraints due to the different wavelengths to be resolved, interpolation is required. The method is applied to a three-dimensional ducted diaphragm with low Mach number flow. Although the configuration is symmetric, this study exhibits a very complex three-dimensional flow behavior. Four different aerodynamic solutions are compared with the Direct Noise Computation performed by Gloerfelt & Lafon. Good agreement is found in terms of mean flow as well as on instantaneous behavior and turbulent intensities. Acoustic computations are performed with different mesh refinement and interpolation methods. Comparison with literature data on similar cases shows the method relevancy.

I. Introduction

In the industrial context, the development of an efficient hybrid noise computation method has to best balance the computing time and the computational resources required to reach a relevant solution. In this work, four aerodynamic solutions obtained with different flow solvers are compared. The complete aeroacoustic process is explained: transfer of aerodynamic data from the CFD mesh to the acoustic mesh, source terms computation, application of filters to damp sources before they reach the acoustic domain boundaries, and resolution of the acoustic propagation problem. In particular, the interpolation of source terms onto the acoustic mesh is detailed. Indeed, depending on the interpolation method chosen, the acoustic mesh in source regions may have to be refined to accurately represent source terms. This has a great impact on the computing time and resources necessary for the acoustic finite element simulation. After introducing the simulation method, its practical implementation is explained, and the interpolation issue is discussed. The method is then applied to the case of a ducted diaphragm with a low Mach number flow, with comparisons between different flow solutions, interpolation methods and acoustic processing. Finally, conclusions are drawn.

*PhD, melanie.piellard@delphi.com.
†Professor, AIAA Senior Member, christophe.bailly@ec-lyon.fr.

II. Simulation method

The simulation method is a two step hybrid approach relying on Lighthill's acoustic analogy,[1] assuming the decoupling of noise generation and propagation. The first step consists of an incompressible Large Eddy Simulation of the turbulent flow field, during which aerodynamic quantities are transiently recorded. In the second step, a variational formulation of Lighthill's Acoustic Analogy discretized by a finite element discretization is solved in the Fourier space, leading to the radiated noise up to the free field thanks to the use of infinite elements.[2]

II.A. Theory

The implementation of Lighthill's acoustic analogy was firstly derived by Oberai *et al*,[3] refer also to Actran User's Guide[2] and Caro *et al*[4] for instance. The starting point is Lighthill's equation:

$$\frac{\partial^2}{\partial t^2}(\rho-\rho_0) - c_0^2 \frac{\partial^2}{\partial x_i \partial x_i}(\rho-\rho_0) = \frac{\partial^2 T_{ij}}{\partial x_i \partial x_j} \tag{1}$$

with

$$T_{ij} = \rho u_i u_j + \delta_{ij}\big((p-p_0) - c_0^2(\rho-\rho_0)\big) - \tau_{ij} \tag{2}$$

where ρ is the density and ρ_0 its reference value in a medium at rest, c_0 is the reference sound velocity, T_{ij} is Lighthill's tensor, u_i are the velocity components, p is the pressure and τ_{ij} is the viscous stress tensor. In our application, with a low Mach number, high Reynolds number flow, the reduced Lighthill's tensor $T_{ij} = \rho u_i u_j$ is considered.

The variational formulation of Lighthill's analogy is then obtained after writing the strong variational statement associated with equation (1), and after integrating by parts along spatial derivatives following Green's theorem. This formulation is actually an equation on the acoustic density fluctuations $\rho_a = \rho - \rho_0$, which reads:

$$\int\limits_{\Omega} \left(\frac{\partial^2 \rho_a}{\partial t^2}\,\delta\rho + c_0^2 \frac{\partial \rho_a}{\partial x_i}\frac{\partial \delta\rho}{\partial x_i} \right) d\mathbf{x} = -\int\limits_{\Omega} \frac{\partial T_{ij}}{\partial x_j}\frac{\partial \delta\rho}{\partial x_i}\, d\mathbf{x} + \int\limits_{\partial\Omega=\Gamma} \frac{\partial \Sigma_{ij}}{\partial x_j}\, n_i\, \delta\rho\, d\Gamma(\mathbf{x}) \tag{3}$$

where $\delta\rho$ is a test function, Ω designates the computational domain, and Σ_{ij} is defined as

$$\Sigma_{ij} = \rho u_i u_j + (p-p_0)\delta_{ij} - \tau_{ij}\,. \tag{4}$$

Two source terms can be distinguished: a volume and a surface contribution. However, when surfaces are fixed, the latest vanishes. Therefore, only the volume source term is considered in this study.

II.B. Practical application

The method consists in coupling a CFD code with a finite element acoustic software where the variational formulation of Lighthill's acoustic analogy is implemented. The main steps of a practical computation, provided that an unsteady solution of the flow field has already been obtained, are as follows:

- flow field analysis allows to determine in which flow region(s) acoustic source terms will be considered; an acoustic mesh is built on the whole region of interest for acoustics, with possibly finer elements in source terms regions;
- the time history of the source terms, or of aerodynamic quantities required to compute it, is stored on the CFD mesh during the CFD computation within the CFD code;
- the source terms, usually computed on the CFD mesh for better accuracy, are interpolated on the coarser acoustic mesh;
- the unsteady source terms are transformed from time to spectral domain;
- the acoustic computation is performed with Actran/LA,[2] taking into account the spectral volume source terms.

In these five steps, the third one, namely the interpolation from the CFD mesh to the acoustic mesh, is of primary importance. Indeed, all the interest of this hybrid aeroacoustic method lies in the decoupling of the noise generation from its propagation. The decoupling makes it possible to adapt each computational step with respect to its efficiency. In particular, the requirements in terms of grid resolution are usually one order of magnitude more severe in the CFD than in the acoustic computation. This is due to the difference in size of acoustic and turbulent wavelengths. Therefore, in order to keep a light and tractable acoustic mesh, an efficient interpolation of source terms from the CFD mesh to the acoustic mesh has to be defined. In this work, two types of interpolation are applied. A classical 4th order Lagrange polynomial interpolation on a fine acoustic mesh will be compared to a conservative interpolation on a coarse acoustic mesh. Conservative interpolation is actually an integration of source terms on the acoustic finite elements. Moreover, it will be shown that the order of finite elements plays an important role when performing integration on a coarse mesh.

III. Case of a ducted diaphragm at low Mach number

III.A. Presentation

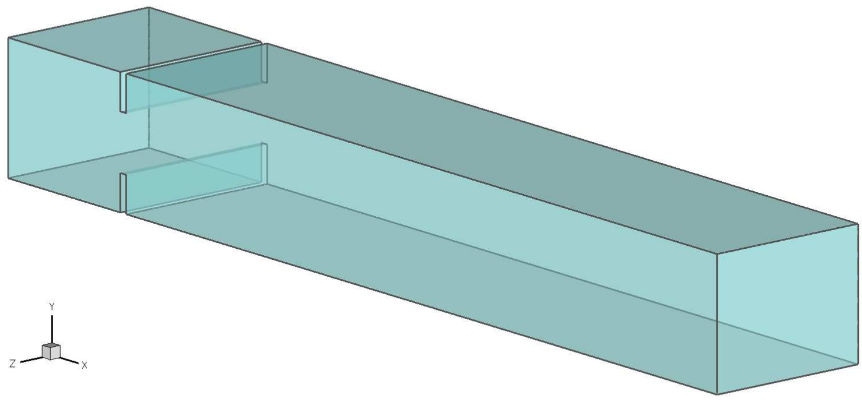

Figure 1. Diaphragm geometry. The x-axis indicates the streamwise flow direction; y- and z-axis respectively indicate the transverse and spanwise directions.

The case of the ducted diaphragm at low Mach number has been described extensively in Piellard *et al.*[5,6] It consists of a duct of rectangular cross-section obstructed by a diaphragm of height h, see Figure 1. The aspect ratio defined as w/h, where w is the spanwise duct extension, is equal to 2.86, and the expansion ratio defined as D/h, where D is the duct height, is 2.29. In this paper, we study the flow and acoustic results for a very low Mach number flow, with the mean velocity $U_0 = 6\,\mathrm{m/s}$ at the inlet, corresponding to Mach number $M = U_0/c_0 = 0.018$. The Reynolds number Re_D based on the inlet velocity U_0 and duct height D, and the Reynolds number Re_h computed at the diaphragm, based on the maximum mean velocity $U_b = 20\,\mathrm{m/s}$ and obstruction height h, are respectively $Re_D = 3.3 \times 10^4$ and $Re_h = 4.8 \times 10^4$.

This geometry is of particular interest since it represents an internal low velocity flow, for which few computational aeroacoustic studies are available. The present work is based on reference results provided by Van Herpe *et al*[7] who performed experiments in order to get the acoustic power radiated by the diaphragm, and by Gloerfelt & Lafon[8] who performed a Direct Noise Computation.

III.B. Four different aerodynamic solutions

As already announced, four different flow solutions are compared in this study. A summary of each calculation's features is proposed here: mesh, discretization and computing code used.

III.B.1. Incompressible slice simulation: Fluent

The first simulation, later denoted slice incompressible simulation, is performed on a slice of the domain consisting in 10% of the real width. A structured mesh of 843,000 cells is built, see Figure 2(a), where the finest cells in the area of the diaphragm and downstream of the diaphragm are of the order $h/70$. An

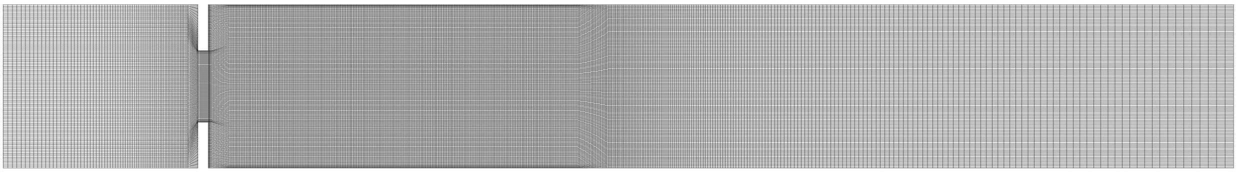

(a) CFD mesh used for Fluent slice computation.

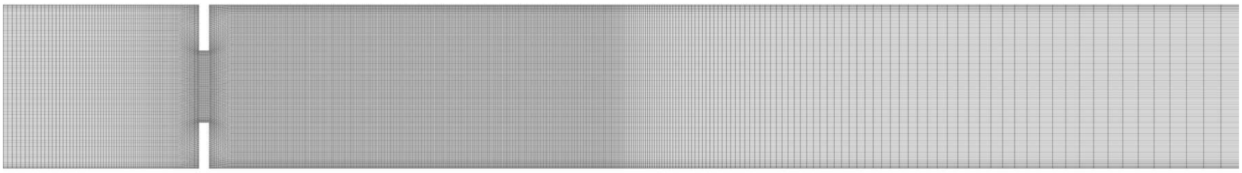

(b) CFD mesh used for Fluent and OpenFOAM 3D computations.

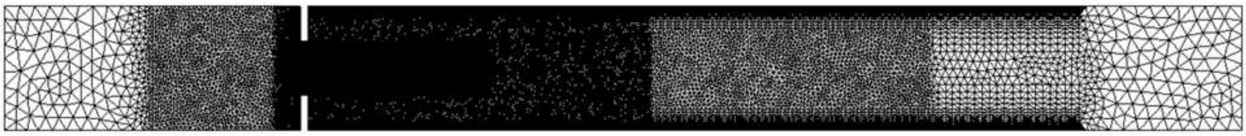

(c) CFD mesh used for Argo 3D computation.

Figure 2. Meshes used for the four CFD simulations.

incompressible Large Eddy Simulation is carried out with the finite volume code Fluent 6.3.26[9] on this mesh. Central differencing is used for the discretization of the momentum equation, PRESTO! for the pressure question, and the pressure-velocity coupling is taken into account via a PISO scheme. The time step satisfies a CFL number less or equal to unity for the smallest cell in the domain, yielding $\Delta t = 5 \cdot 10^{-7}$ s.

III.B.2. Incompressible 3D simulation: Fluent

In this second study, an incompressible Large Eddy Simulation is performed with Fluent 6.3.26[9] on the complete three-dimensional domain. The mesh, counting 8 million cells, is very similar to the previous one, see Figure 2(b), structured with finest cells downstream of the diaphragm of the order $h/70$. Discretization schemes are the same as for the incompressible slice simulation. The chosen time step $\Delta t = 10^{-5}$ s corresponds to a maximum CFL number of 0.78.

III.B.3. Incompressible 3D simulation: OpenFOAM

In this second study, an incompressible Large Eddy Simulation is performed with OpenFOAM[10] on the complete three-dimensional domain. The mesh is exactly the same as the previous one. Central differencing and second order schemes are used for space discretization. Time discretization is performed with a Crank-Nicholson scheme, i.e. a second order bounded implicit scheme. The chosen time step $\Delta t = 10^{-5}$ s corresponds to a maximum CFL number of 0.78.

III.B.4. Compressible 3D simulation: Argo

In this last study, the code Argo[11,12] developed at Cenaero has been used. Argo has a hybrid finite volume/finite element formulation, where convective terms are computed in a finite volume framework using linearly reconstructed face values (typically a Roe's approximate Riemann solver), and diffusive terms are computed using the Galerkin P1 finite element approximation. Full implicit time integration is performed using a second order 3-points Backward-Differencing scheme. For LES-type applications, Argo uses a second-order non-dissipative central scheme which conserves the kinetic energy at the discrete level. For industrial high-Reynolds number flow applications, a hybrid formulation based on the Detached Eddy Simulation approach derived from the one-equation Spalart-Allmaras model is implemented. In order to achieve a dis-

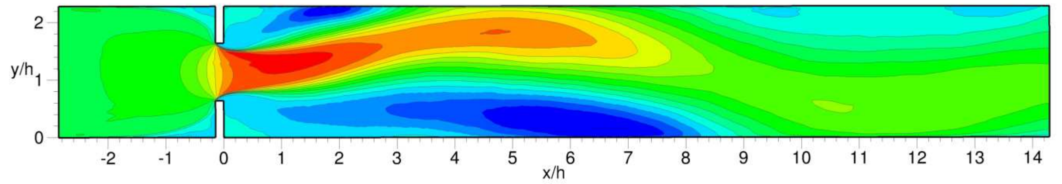

(a) Fluent slice simulation.

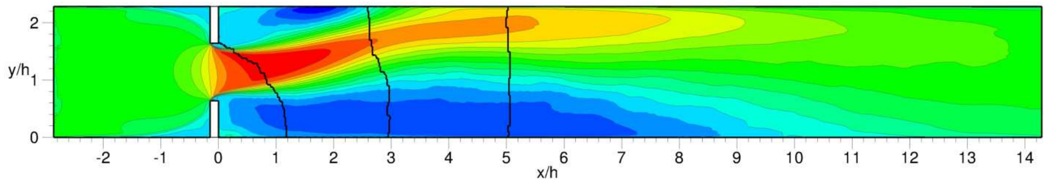

(b) Fluent 3D simulation.

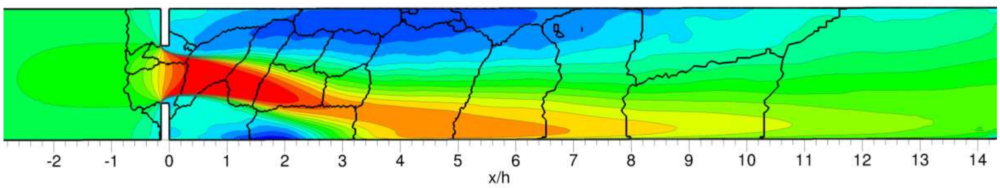

(c) Argo 3D simulation.

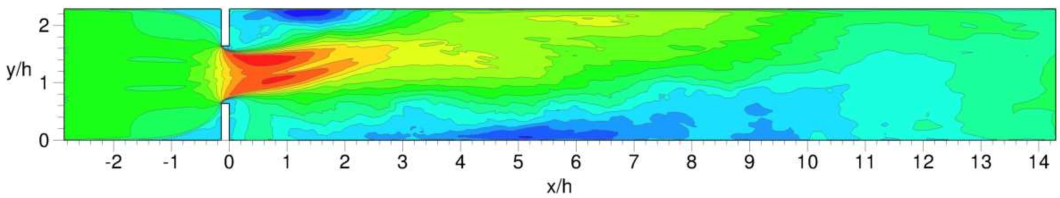

(d) OpenFOAM 3D simulation.

Figure 3. Mean streamwise velocity fields u/U_b in the XY midplane for the four LES simulations, where the maximum mean velocity $U_b = 20\,\mathrm{m/s}$ is used for normalization. The bold black lines delimit the boundaries of the partitions used in parallel runs.

cretization in accordance with the flow physics and the modeling strategy, the upwind scheme is used in the RANS region while the kinetic energy central scheme is active in the LES region.

An unstructured tetrahedral mesh is built on the same geometry as previously, with slight extensions upstream and downstream. The mesh, shown in Figure 2(c), is refined by blocks and counts a total of 5.6 million nodes and 33.4 million elements. Fine cells are found just downstream of the diaphragm, with a cell size of order $h/70$. Finer cells of size $h/140$ are locally placed around diaphragm edges, and a local near-wall refinement leads to the finest cell size of $h/3500$. In this case, a RANS-LES simulation using Detached Eddy Simulation (DES) is chosen: Reynolds Averaged Navier-Stokes modeling is applied near the walls if the local refinement is not enough for a pure wall-resolved LES, and LES is applied away from the walls and near the walls if the mesh sufficiently refined. A low Reynolds number correction of the DES model is activated as the Reynolds number is moderate. The time step is $\Delta t = 5 \cdot 10^{-5}\,\mathrm{s}$.

III.C. Flow field analysis

III.C.1. Mean flow field

Figure 3 presents the mean streamwise velocity fields for the four simulations. Mean flow results of the incompressible slice simulation favorably compare to the Large Eddy Simulation simulation of Gloerfelt & Lafon,[8] despite the truncation in the third direction. The main effect of the spanwise truncation is

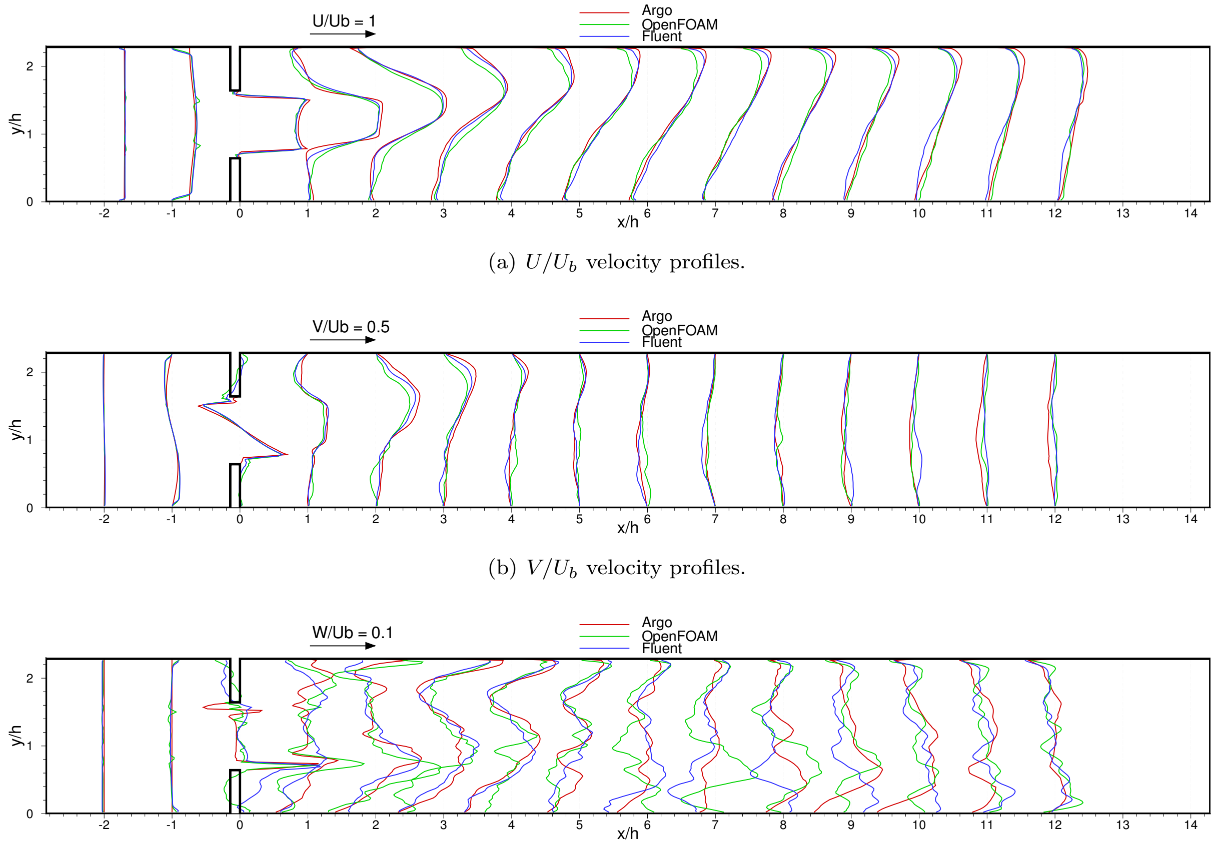

(a) U/U_b velocity profiles.

(b) V/U_b velocity profiles.

(c) W/U_b velocity profiles.

Figure 4. Mean velocity fields in the XY midplane for the three 3D LES simulations.

to constrain the flow to an exaggerated two-dimensional behavior, erasing the complex three-dimensional developments. In addition, a secondary attachment to the bottom wall occurs around $x/h = 10$, which is highly questionable, as most authors report such a feature downstream, from $x/h = 20$. Regarding the 3D simulations with Fluent and Argo, no major difference is noticed with Gloerfelt& Lafon[8] when analyzing the mean flow fields; the position and extent of recirculation zones and boundary layers are satisfactory. However, OpenFOAM results exhibit a less smooth velocity field, suggesting that the flow may not be totally converged. The complex three-dimensional behavior of the flow for Fluent 3D simulation is described thoroughly in Piellard *et al*[5] and will not be reviewed here.

It is interesting to note that all published numerical experiments performed on planar sudden expansions report a natural evolution of the flow toward asymmetry. This is also true using Reynolds Averaged Navier-Stokes simulations, provided that the geometric and flow conditions are favorable to bifurcation, and that a transient computation is led. This phenomenon is called the Coanda effect. From the compared analysis of experimental and simulation bifurcation diagrams, Fearn *et al*[13] conclude that, considering the overall agreement in resulting diagrams, the bifurcation observed is a fundamental property of the Navier-Stokes equations. For a similar experimental and numerical study of a plane sudden expansion, Durst *et al*[14] always assume a symmetric flow configuration. As the resulting flow always present a bifurcation without geometric inlet disturbances, the authors attribute the asymmetry to truncation errors which prevent a zero transverse velocity at the symmetry plane. In the present simulations, the asymmetry causes the flow to attach to the top wall in all cases, except for Argo simulation, where flow attach to the bottom wall. Note also that the bifurcation toward asymmetry happened much later (in the computation time frame) for OpenFOAM simulation than for the other ones. As the schemes are more accurate, it was necessary to add fluctuations at inlet to trigger the transition. The schemes' accuracy may also explain the flow convergence not achieved at this point of the simulation, corresponding to one integral flow time after introducing fluctuations at inlet.

Figure 4 presents a comparison of mean flow profiles in the XY midplane, for all three dimensional

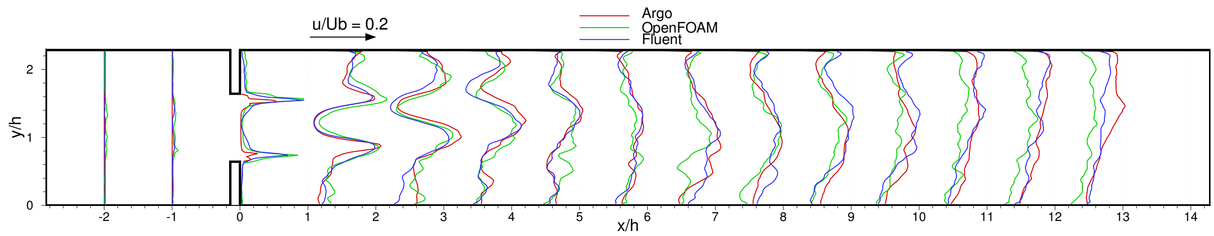

(a) u'/U_b velocity profiles.

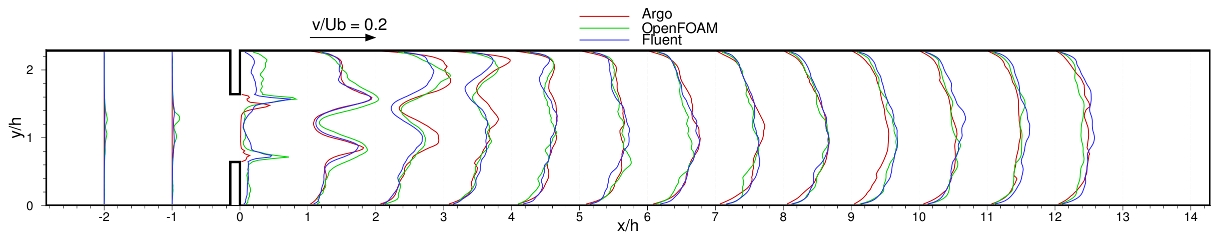

(b) v'/U_b velocity profiles.

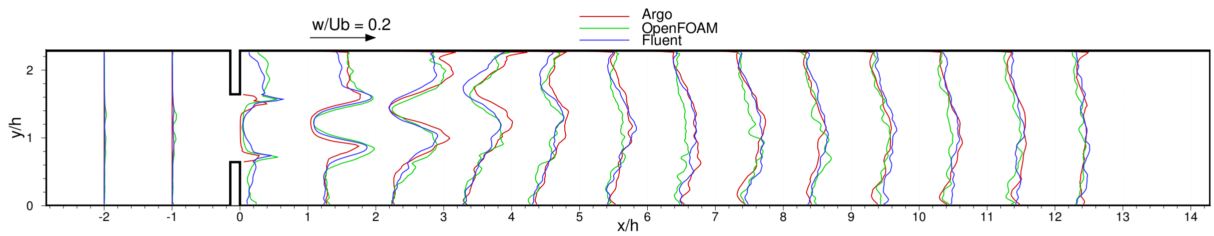

(c) w'/U_b velocity profiles.

Figure 5. Turbulence intensities in the XY midplane for the three 3D LES simulations. Turbulent intensities are computed as $u' = \sqrt{\overline{u^2}}$ and normalized by U_b.

simulations. Note that the data from Argo simulation have been mirrored with respect to the y-axis in order to compare with data from Fluent and OpenFOAM. From these plots, it is clear that the streamwise and spanwise mean velocity components are very similar for the three cases, qualitatively as well as quantitatively. The maximum values of U/U_b follow the general direction of the flow toward the top wall, and the largest back flow is located in the core of the large recirculation zone, near the walls for $3 \leq x/h \leq 8$, reaching a value of $20\%U_b$ as noticed in previous studies.[14–17] Small differences are noticed on the streamwise velocity profile of OpenFOAM calculation, for $x/h = -1$ and -2: these profiles differ from Fluent and Argo upstream the diaphragm, exhibiting a boundary-layer behavior. These fluctuations are also visible on Figure 3(d).

Local minima and maxima of transverse mean velocity, reaching $\pm 30\%U_b$ are found upstream the diaphragm lips, where the flow is accelerated through the contraction; in the outlet duct, a maximum of $25\%U_b$ is located in the lower shear layer just before the jet flow attaches the top wall.

Spanwise velocity profiles show very different behaviors from one simulation to the other, in terms of shape as well as in terms of levels. This cannot be confirmed or infirmed though, since nothing has been published regarding the spanwise velocity evolution; in addition, it is closely linked to the three-dimensional flow development in the ducted diaphragm and could probably not be compared with a plane sudden expansion configuration.

III.C.2. Turbulent intensity field

Figure 5 presents a comparison of turbulent intensities profiles in the XY midplane, for all three dimensional simulations. These plots show a significant anisotropy, with streamwise intensity levels in general higher than the transverse and spanwise ones. Local maxima are found in the shear layers before the attachment. The maximum value of the r.m.s. streamwise turbulence intensity is around $24\%U_b$, consistent with that reported by Casarsa & Giannattasio[15] and Escudier *et al*;[17] resulting streamwise turbulence in the second

Acoustic mesh	Number of nodes	Number of elements
2D	44,234	86,162
3D refined	711,301	1,494,320
3D fine linear	45,738	40,600
3D fine linear (Argo)	60,480	53,860
3D fine quadratic	177,645	40,600
3D coarse quadratic	43,243	9,168

Table 1. Number of elements and nodes (or degrees of freedom) for each acoustic mesh.

half of the duct has a 15% mean intensity, also consistent with previous studies.

The transverse turbulence intensity reaches a maximum between 16 and 22%U_b in the upper shear layer, consistent with Escudier *et al*[17] and sligthly higher than that of Casarsa & Giannattasio;[15] far downstream, the mean transverse turbulence intensity is still 10% of U_b. The spanwise turbulence intensity reaches a maximum between 18 and 22%U_b in the upper shear layer; far downstream, the mean spanwise turbulence intensity is still 8% of U_b for all simulations.

III.D. Acoustic simulation

On the inlet and outlet faces, acoustic duct modes are imposed, such that only outgoing free modes can exist; therefore, free modes in the $-x$-direction are imposed at inlet, and free modes in the $+x$-direction are imposed at outlet. The MUMPS solver is chosen for resolution. After interpolation, described for each solution below, source terms are Fourier transformed, and a Hanning window is applied. In all cases, spatial filtering is also applied to source terms in the second half of the outlet duct to ensure a smooth transition to zero of the source terms toward the domain exit.

III.D.1. Influence of the interpolation scheme

In order to study interpolation effects, three acoustic meshes are built and used with the data from Fluent slice and 3D simulations, with different interpolation methods.

No interpolation: 2D acoustic computation

A first two dimensional acoustic computation is performed, using the data recorded in the central XY plane of the incompressible slice CFD domain. The acoustic mesh, shown in Figure 6(a), is identical to the CFD mesh in the first part of the outlet duct and in the diaphragm region, and coarser elsewhere; it is valid up to 10 kHz. As the acoustic mesh is identical to the CFD mesh where source terms are computed, no interpolation is required to input the source terms in the acoustic computation; a basic mapping is simply performed.

Lagrange interpolation

The second acoustic mesh is three-dimensional. It is very refined in the first part of the outlet duct, with the cell size equal to twice the CFD mesh size, see Figure 6(b). Because the acoustic mesh is not identical to the CFD mesh in source regions, interpolation is required to define acoustic source terms on the acoustic mesh. Source terms are thus computed on the CFD mesh, and a non conservative 4th order Lagrange polynomial interpolation is performed.

Conservative interpolation: integration

The last three dimensional acoustic mesh is built only with acoustic wave propagation requirements, without considering the presence or not of source terms. The mesh is uniform with a cell size of $h/7$ in the whole domain, see Figure 6(c). In this case, where interpolation is required, a conservative interpolation scheme developed by Free Field Technologies[18] is applied. This interpolation consists in integrating source terms over the acoustic finite elements, preserving the energy contained in the source terms:[19] source terms are

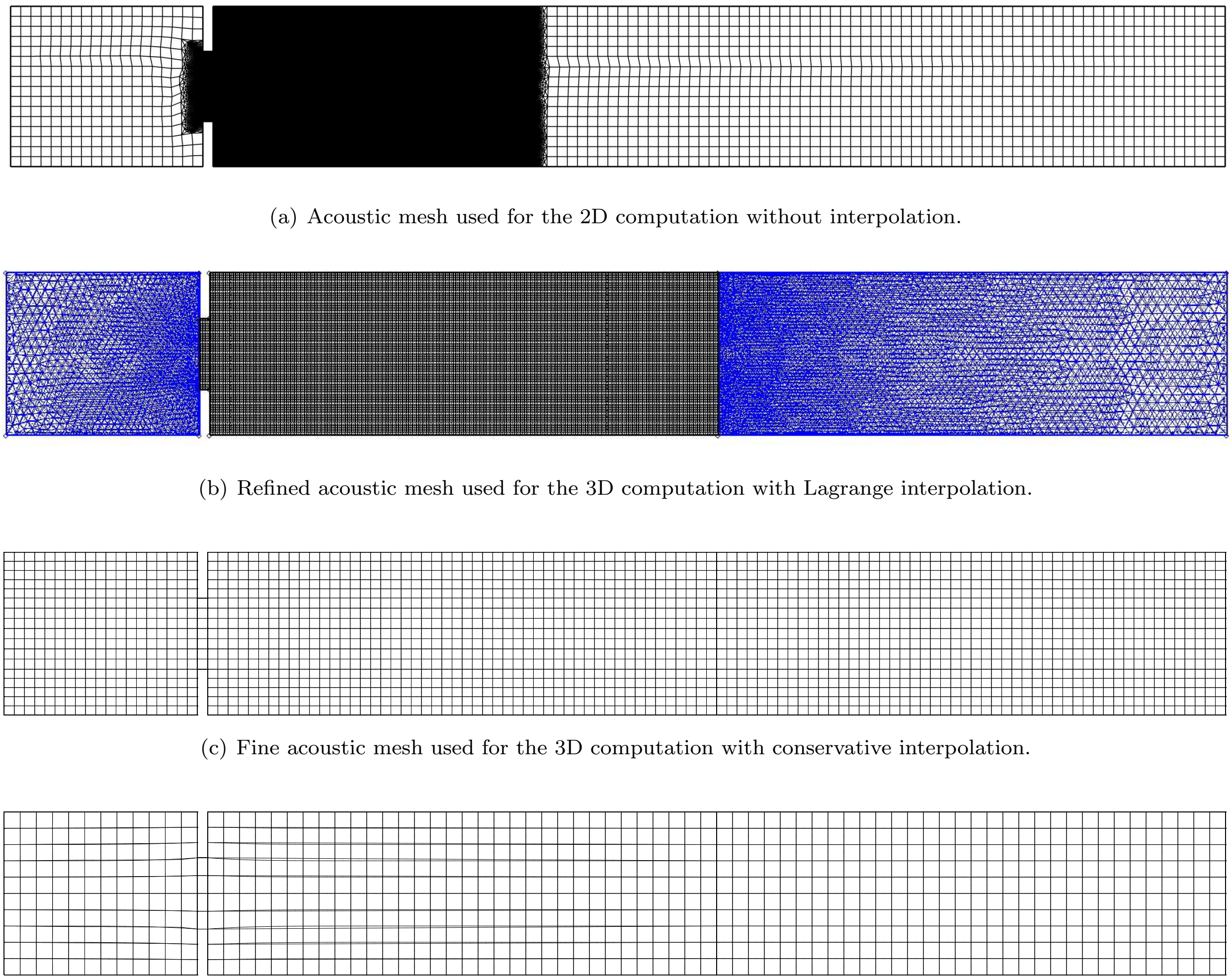

(a) Acoustic mesh used for the 2D computation without interpolation.

(b) Refined acoustic mesh used for the 3D computation with Lagrange interpolation.

(c) Fine acoustic mesh used for the 3D computation with conservative interpolation.

(d) Coarse acoustic mesh used for the 3D computation with conservative interpolation.

Figure 6. Meshes used for acoustic simulations.

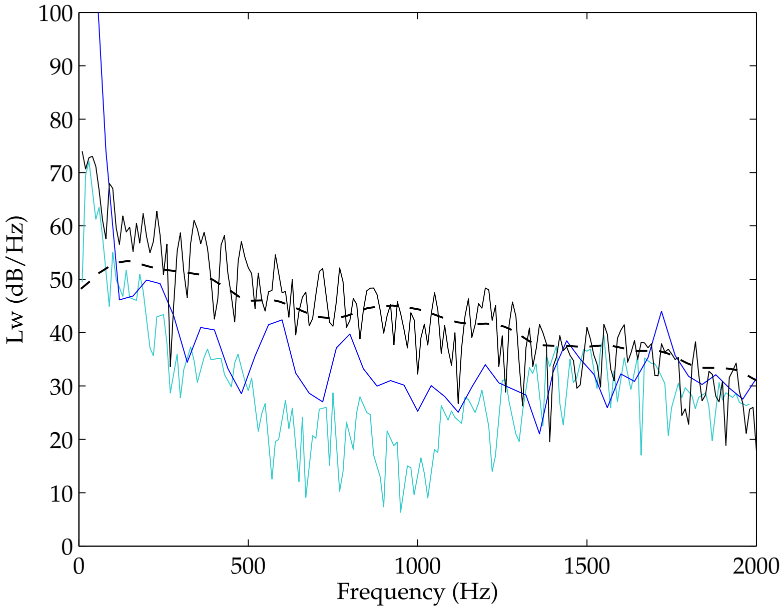

Figure 7. Acoustic power radiated at the duct outlet. Influence of the interpolation scheme. − − −: reference results of Gloerfelt & Lafon,[8] ——: 2D acoustic computation without interpolation, ——: 3D acoustic computation with Lagrange interpolation, ——: 3D acoustic computation with conservative interpolation i.e. integration.

computed on the fluid mesh, and for each acoustic node, the final right hand side of Equation 3 is obtained by summing the contributions of the surrounding fluid cells, taking the acoustic elements shape functions into account.

Results

Acoustic results are given in terms of acoustic power radiated at the duct outlet in Figure 7. It appears that, in spite of the limitations of the CFD slice computation, the corresponding two dimensional acoustic simulation, without interpolation, gives relevant results, with in particular the spectrum broadband shape similar to the reference Direct Noise Computation[8] over the whole frequency range [0–2000] Hz.

By contrast, three dimensional results on the refined acoustic mesh, with Lagrange polynomials interpolation, presents a broadband spectrum shape very different from the reference; a loss of energy in the frequency range [100–1400] Hz is particularly visible. This loss of energy is attributed to the information loss during interpolation, where roughly only $1/8^{th}$ of the source terms information was kept, which corresponds to a decimation by 2 in each space direction from the CFD to the acoustic mesh.

Better results are obtained with the fine linear three dimensional acoustic mesh using integrated source terms. Note that in this last computation, only 50 ms of signal was available, while 100ms were considered in previous simulations. The mandatory signal windowing (Hanning) has thus a great influence, and better results are expected with a longer simulation time.

III.D.2. Influence of the finite elements order

In order to improve the results obtained with the CFD data integrated onto the fine acoustic mesh, the order of acoustic finite elements is increased, and quadratic elements are used on the same mesh. Doing this roughly multiplies by a factor of 4 the number of integration nodes, in three dimensions; see Table III.D for exact mesh sizes. The computing time is also considerably increased, and, as Figure 8 attests it, the accuracy is not significantly increased. Source terms are now integrated on the quadratic finite elements, taking intermediate points into account, which should increase the fidelity of their representation, while whit is not clearly visible on the spectra. Very high levels are still present at low frequencies, and levels are lower than the reference in the range [200–1500] Hz. In order to understand the minimum discretization required using quadratic elements, another quadratic acoustic mesh is build with a cell size of $h/4$ in the whole domain,

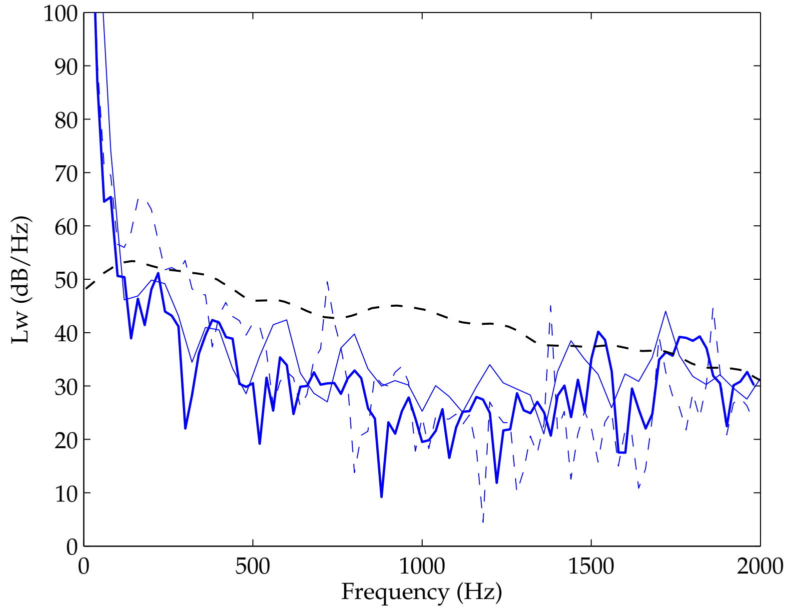

Figure 8. Acoustic power radiated at the duct outlet. Influence of the interpolation order using Fluent 3D data. – – –: reference results of Gloerfelt & Lafon,[8] ——: 3D acoustic computation with conservative interpolation on the fine linear mesh, ——: 3D acoustic computation with conservative interpolation on the fine quadratic mesh, – – –: 3D acoustic computation with conservative interpolation on the coarse quadratic mesh.

see Figure 6(d), roughly dividing by 4 the number of elements with respect to the fine acoustic mesh. Results are to other spectra, with no significant difference. Therefore, it can be concluded that, all these meshes, namely a fine linear mesh, a fine quadratic and a coarse quadratic mesh, provide similar results, none of them being closer to the reference spectrum.

III.D.3. Effect of the CFD resolution

A comparison of acoustic results obtained using both incompressible (Fluent and OpenFOAM) and compressible (Argo) fluid data is presented in Figure 9. The same fine acoustic mesh as described previously is used for all spectra, and source terms are obtained by conservative interpolation, i.e. integration. Different mesh size is reported in Table III.D for Argo fine acoustic mesh because of the domain extension, slightly increased to fit the fluid domain, the mesh size $h/7$ being kept identical to the fine acoustic mesh. Results from the compressible code Argo are very similar to the ones obtained with Fluent using the quadratic fine acoustic mesh, which suggests that the refined fluid solution may not improve acoustic results; in this case, it was not possible to perform the integration on a quadratic mesh due to hardware memory limitations. In particular, the finer fluid resolution of the compressible model in the diaphragm area does not provide any improvement on acoustic results. In the low frequency range, very high levels are still present. Results using OpenFOAM data integrated over the fine quadratic acoustic mesh follow Fluent and Argo spectra up to 700 Hz. Then, a slight improvement is noticed with higher levels up to 1000 Hz, and up to the duct first mode at 1700 Hz, a pronounced acoustic level decrease occurs. This is attributed to the non stabilized flow field, as described in III.C.1.

III.D.4. Origin of the low frequency peak

On all the spectra obtained using the present method, high levels are obtained in the low frequency range, below 100 Hz. The highest levels were produced using integration, while reasonable peaks were produced using a sampling procedure or a non-conservative interpolation. This kind of peak is not present at all in the reference spectrum, the Direct Noise Computation performed by Gloerfelt & Lafon.[8] In order to understand its origin, an experimental spectrum obtained by Van Herpe[7] is plotted in Figure 10. In this experiment, the domain is the same (same diaphragm and duct sections), but the inlet velocity is 14 m/s instead of 6 m/s in

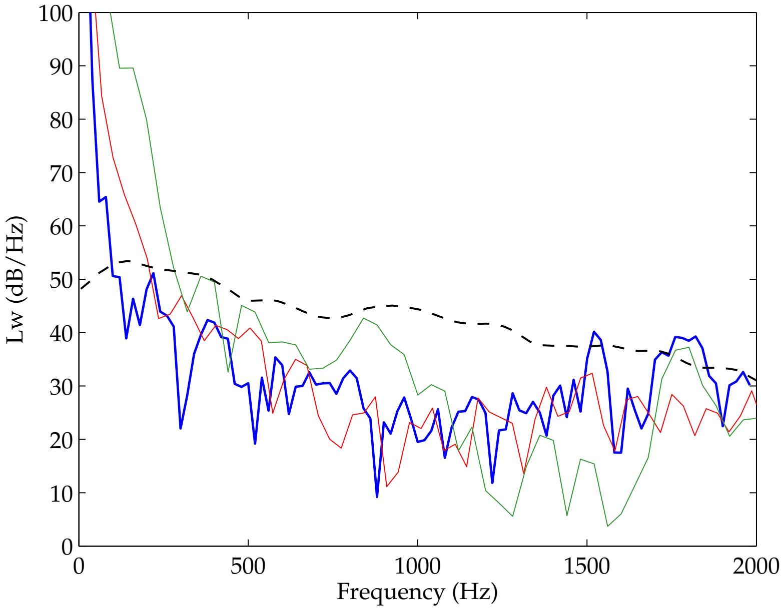

Figure 9. Acoustic power radiated at the duct outlet. Effect of the CFD resolution. – – –: reference results of Gloerfelt & Lafon,[8] ——: 3D acoustic computation with conservative interpolation of Fluent data on the fine quadratic mesh, ——: 3D acoustic computation with conservative interpolation of Argo data on the fine linear mesh, ——: 3D acoustic computation with conservative interpolation of OpenFOAM data on the fine quadratic mesh.

the present study. This experimental acoustic power spectrum also exhibits strong low frequency levels below 100 Hz. Even if the absolute levels cannot be compared because of the mass flow difference, this comparison shows the physical origin of the low frequency peak.

IV. Conclusion

In this work, the focus is put on the comparison of different strategies of source term interpolation from the CFD mesh to the acoustic mesh, and on the comparison of results obtained using different fluid codes. With no surprise, the best acoustic results are obtained when fluid and acoustic meshes are identical, requiring no interpolation at all for the source terms; this corresponds to the study on a slice of the domain, where very good results were obtained from a two-dimensional acoustic computation, with all limitations of the fluid simulation. When interpolation is required, which is usually the case since an acoustic mesh as fine as the fluid mesh is not tractable in most applications, even a high order Cartesian interpolation is not sufficient to provide relevant results; the loss of information during non conservative interpolation cannot be retrieved by increasing the interpolation order. Besides, the use of a conservative interpolation, consisting of source terms integration, allows a more accurate representation of the source terms while preserving their energy. This last solution gives better results than classical interpolation. A study of the acoustic finite elements order did not favor quadratic elements, while it was expected to improve the results due to the better discretization of source terms. In addition, the comparison of previously obtained Fluent data with results obtained by Argo and OpenFOAM is successful on the case of a ducted diaphragm at low Mach number flow. While CFD mesh and solvers are very different, mean as well as instantaneous aerodynamic quantities are similar, except on OpenFOAM data where some differences are noticed. Regarding acoustic spectra, the results are also very similar, except using OpenFOAM data for which the medium frequency range is not well predicted. However, the comparison of present results with the reference simulation still exhibits important differences in terms of levels, as well as regarding the shape of spectra. Only a thorough experimental study could eliminate all these doubts and provide a conclusion on the performance of the presented Computation Aeroacoustic method.

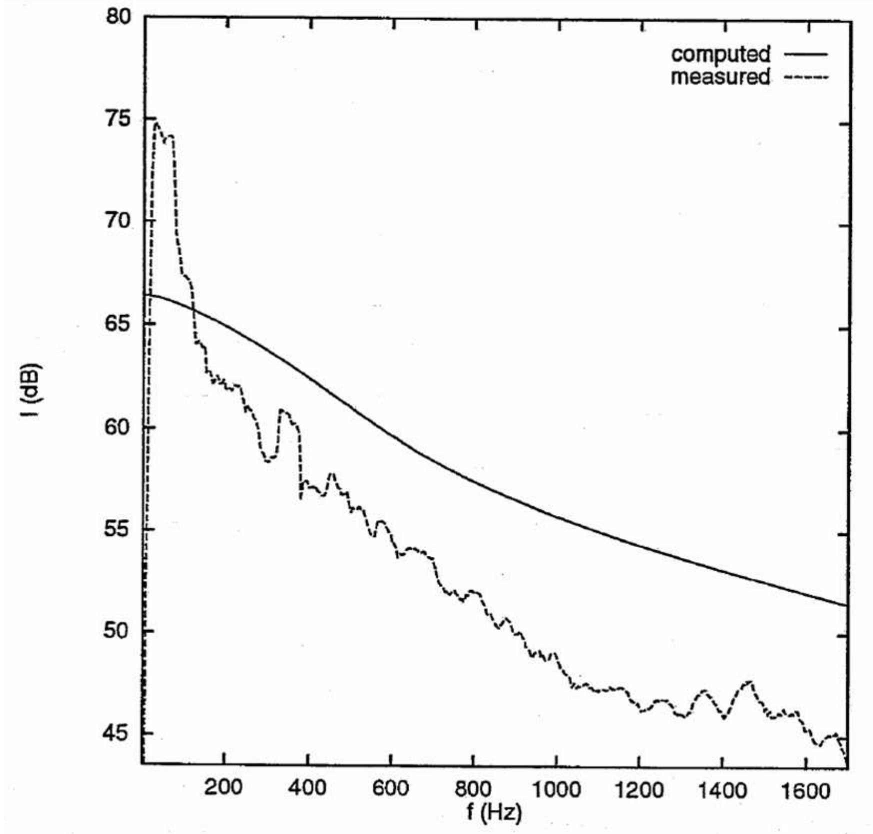

Figure 10. Acoustic power radiated at the duct outlet. Results obtained by Van Herpe[7] for an inlet velocity of 14 m/s, in the same geometry. – – –: measurements, ——: simulation.

Acknowledgments

The first author would like to greatly acknowledge CENAERO for providing CFD data obtained with their in-house code Argo, as well as Free Field Technologies for their help using their software Actran.

References

[1]Lighthill, M., "On sound generated aerodynamically. Part I: General theory," *Proceedings of the Royal Society of London*, Vol. A211, 1952, pp. 564–587.

[2]Free Field Technologies, *Actran/TM and Actran/LA 2007, User's Manual*, 2007.

[3]Oberai, A. A., Roknaldin, F., and Hughes, T. J. R., "Computational procedures for determining structural-acoustic response due to hydrodynamic sources," *Computer Methods in Applied Mechanics and Engineering*, Vol. 190, 2000, pp. 345–361.

[4]Caro, S., Ploumhans, P., and Gallez, X., "Implementation of Lighthill's Acoustic Analogy in a finite/infinite elements framework," *AIAA Paper 2004–2891*, 2004, 10th AIAA/CEAS Aeroacoustics Conference.

[5]Piellard, M. and Bailly, C., "Validation of a hybrid CAA method. Application to the case of a ducted diaphragm at low Mach number," *14th AIAA/CEAS Aeroacoustics Conference, May 5–7, Vancouver, Canada*, , No. AIAA Paper 2008-2873, 2008.

[6]Piellard, M., *A hybrid method for Computational AeroAcoustics applied to confined geometries*, Ph.D. thesis, Ecole Centrale de Lyon, 2008, In French.

[7]Van Herpe, F., *Computational aeroacoustics for turbulent duct flow*, Ph.D. thesis, Ecole Centrale de Paris, 1994.

[8]Gloerfelt, X. and Lafon, P., "Direct computation of the noise induced by a turbulent flow through a diaphragm in a duct at low Mach number," *Computers & Fluids*, Vol. 37, No. 4, 2008, pp. 388–401.

[9]Fluent Inc., *Fluent 6.3 User's Guide*, Sept. 2007.

[10]OpenCFD Limited, *OpenFOAM 1.6 User's Guide*, 2009.

[11]Georges, L., Winckelmans, G., and Geuzaine, P., "Improving shock-free compressible RANS solvers for LES on unstructured meshes," *Journal of Computational and Applied Mathematics*, Vol. 215, 2008, pp. 419–428.

[12]Georges, L., Hillewaert, K., Capart, R., Thomas, J.-F. andLouagie, T., and Geuzaine, P., "RANS-LES simulations

around a complete landing geometry," *Proceedings of the 7th International ERCOFTAC Symposium on Engineering Turbulence Modelling and Measurements*, 2008.

[13]Fearn, R. M., Mullin, T., and Cliffe, K. A., "Nonlinear flow phenomena in a symmetric sudden expansion," *Journal of Fluid Mechanics*, Vol. 211, 1990, pp. 595–608.

[14]Durst, F., Pereira, J. C. F., and Tropea, C., "The plane symmetric sudden-expansion flow at low Reynolds numbers," *Journal of Fluid Mechanics*, Vol. 248, 1993, pp. 567–581.

[15]Casarsa, L. and Giannattasio, P., "Three-dimensional features of the turbulent flow through a planar sudden expansion," *Physics of Fluids*, Vol. 20, 2008.

[16]De Zilwa, S. R. N., Khezzar, L., and Whitelaw, J. H., "Flows through plane sudden-expansions," *International Journal for Numerical Methods in Fluids*, Vol. 32, 2000, pp. 313–329.

[17]Escudier, M. P., Oliveira, P. J., and Poole, R. J., "Turbulent flow through a plane sudden expansion of modest aspect ratio," *Physics of Fluids*, Vol. 14, No. 10, 2002, pp. 3641–3654.

[18]Free Field Technologies, *Actran 2009 for Aeroacoustics, User's Manual*, 2009.

[19]Caro, S., Detandt, Y., Manera, J., Toppinga, R., and Mendonça, F., "Validation of a new hybrid CAA strategy and application to the noise generated by a flap in a simplified HVAC duct," *AIAA Paper 2009–3352*, 2009, 15th AIAA/CEAS Aeroacoustics Conference.